Chinese Chemical Letters 33 (2022) 1412–1416

Contents lists available at ScienceDirect

Chinese Chemical Letters

journal homepage: www.elsevier.com/locate/cclet

Heat treatment-induced Co^{3+} enrichment in CoFePBA to enhance OER electrocatalytic performance

Wenhui Hu[a], Mingbo Zheng[a,b,*], Huiyu Duan[a], Wei Zhu[a], Ying Wei[a], Yi Zhang[a], Kunming Pan[c], Huan Pang[a,*]

[a] School of Chemistry and Chemical Engineering, Yangzhou University, Yangzhou 225002, China
[b] College of Materials Science and Technology, Nanjing University of Aeronautics and Astronautics, Nanjing 210016, China
[c] National Joint Engineering Research Center for Abrasion Control and Molding of Metal Materials, and Henan Key Laboratory of High-temperature Structural and Functional Materials, Henan University of Science and Technology, Luoyang 471003, China

ARTICLE INFO

Article history:
Received 1 July 2021
Revised 2 August 2021
Accepted 7 August 2021
Available online 12 August 2021

Keywords:
Prussian blue analogues
Co-based catalysts
Porous framework
Electrocatalyst
Oxygen evolution reaction

ABSTRACT

Increasing active metal sites is a valid approach to improve the catalytic activity of the catalyst. Co^{3+} is the main active metal site of Co-based catalysts. In this research work, through the partial transformation of CoFePBA (CFP) *via* low-temperature heat treatment, the effective control of the Co^{3+}/Co^{2+} ratio has been achieved. The partial transformation strategy of low-temperature heat treatment can not only maintain the original framework structure of CFP, but also increase more active sites. The characterization results show that the CFP-200 sample obtained *via* heat treatment at 200 °C for 2 h under N_2 atmosphere has the highest Co^{3+}/Co^{2+} ratio. As an oxygen evolution reaction electrocatalyst, CFP-200 shows the best electrocatalytic activity among all samples. In 1.0 mol/L KOH electrolyte, the overpotential is 312 mV at a current density of 10 mA/cm^2. Therefore, low-temperature heat treatment provides an effective method for preparing low-cost and high-efficiency electrocatalysts.

The development of sustainable, clean and efficient energy production has long been considered as a promising strategy to satisfy the energy needs of modern society [1–4]. Electrocatalytic oxygen evolution reaction (OER) has important significance for energy conversion technologies, such as solar energy utilization [5,6], water splitting [7,8] and rechargeable metal air battery [9–12]. OER is a very important reaction in electrolysis of water [13]. Because it is a four-electron proton coupling reaction, the reaction kinetics is slow and requires higher energy [14,15]. Ideally, the potential required to trigger the reaction should be equal to the potential when the reaction is in equilibrium. However, due to the existence of reaction energy barriers, the potential applied to the reaction is often much higher than the potential required in equilibrium. At present, the most effective OER catalysts are noble metal iridium and ruthenium oxides (IrO_2 and RuO_2, *etc.*). However, their scarcity and high cost severely limit the large-scale application [16,17]. The development of low cost and high activity OER electrocatalysts is of great significance for sustainable energy conversion and storage.

Prussian Blue (PB) is the oldest artificial coordination polymer based on cyanide. Its iron species can be replaced with other transition metals (such as Co, Ni and Mn) to prepare a series of Prussian blue analogues (PBA), which general formula is $A_xM_a[M_b(CN)_6]_y{\cdot}nH_2O$, where A and M_a/M_b represent alkaline metal cations (K^+/Na^+) and transition metal cations (Fe^{2+}, Co^{2+}, Ni^{2+}, Mn^{2+}, *etc.*), respectively. Due to its characteristics of porosity, adjustable composition, simple preparation, versatility, and good stability, PBA has been widely studied in the field of energy, such as LIBs [18,19], SIBs [20–22], aqueous battery [23,24], supercapacitor [25–28] and electrocatalysis [29]. In particular, CFP has strong stability in a large pH range, the mixed-valence state of Co and Fe elements is conducive to the electronic conductivity of the material. Also, the frame structure of CFP is conducive to the rapid ion transport. Therefore, CFP was widely used in the design of OER electrocatalyst. For example, Han's group prepared $Co_3[Fe(CN)_6]_2$ array with one-dimensional structure *via* ion-exchange method. The electrocatalytic OER results showed that the overpotential at the current density of 1 mA/cm^2 was only 340 mV (without IR compensation) [30]. Mascaros *et al.* synthesized CFP thin film electrocatalysts using a chemical etching process. These thin films can generate higher order of electrocatalytic current and have excellent stability [31]. Because of the advantages of three-dimensional

* Corresponding authors at: School of Chemistry and Chemical Engineering, Yangzhou University, Yangzhou 225002, China.
E-mail addresses: zhengmingbo@nuaa.edu.cn (M. Zheng), huanpangchem@hotmail.com, panghuan@yzu.edu.cn (H. Pang).

https://doi.org/10.1016/j.cclet.2021.08.025
1001-8417/

skeleton structure, controllable original particle size, high specific surface area, and good stability, CFP-derived nanostructured materials also have a good application prospect in the field of electrochemical energy storage and conversion. Yuan's group combined CFP-derived bimetallic oxides with three-dimensional graphene, providing a general method for excellent integrated anode material for lithium-ion batteries [32]. He *et al.* used CFP as the precursor to prepare a mesoporous cobalt/iron-phosphorus selenide nanocomposite (CoFe-Se-P) with phosphating and selenization strategies [33]. The material has high-efficiency and long-lasting bifunctional catalysis for electrochemical hydrogen evolution reaction (HER) and OER. Although there are many studies on the preparation of nanostructured inorganic functional materials based on CFP derivatization, most of them are based on the complete transformation, and the framework structure of CFP is completely destroyed. However, there are few reports about the partial transformation of CFP derivatization.

In recent years, transition metal-based (Co, Fe, Ni, Mn, Cu, Zn, *etc.*) electrocatalysts have been studied extensively [34–37]. In particular, cobalt-based electrocatalysts show good application potential due to the unique 3D orbital electron arrangement and adjustable electrocatalytic activity of Co element [38,39]. Metal ions often play important roles in the catalytic process of OER. Co^{3+} is the main active site in the process of adsorption, activation and desorption for cobalt-based electrocatalysts [40–43]. Mu *et al.* synthesized 2D porous Co_3O_4 nanosheets with abundant stratified pores and a high Co^{3+}/Co^{2+} ratio. The sample showed excellent OER catalytic performance in 1.0 mol/L KOH solution, with an overpotential of only 270 mV at 10.0 mA/cm^2 [44]. Liu *et al.* developed a plasma activation strategy to synthesize a novel $Co_3(PO_4)_2$ nanosheet array [45]. Because the surface is rich in Co^{3+}, it is used for the overall water decomposition reaction, showing an efficient bifunctional electrocatalytic effect. At present, the exploration of the effect of Co^{3+}/Co^{2+} ratio of CFP on its OER electrocatalytic performance has not been reported.

The heat treatment of material is a common method for the preparation of function materials. These heat treatment derived materials have attracted considerable attention in catalysis [46,47], sensing [48] and energy conversion [49]. Xu's group developed a strategy to strengthen the metal-nanoparticles/MOF interaction by controlling the thermal transition. The prepared metal composite material has a transition state structure between porous MOF and metal oxide, which can improve the catalytic performance in low-temperature oxidation of carbon monoxide (CO) [47]. In addition, Zhu *et al.* used a simple low-temperature calcination method to achieve partial deionization of ZIF-67. The heat treatment resulted in the loss of ZIF-67 partial ligand, the rupture of Co-N bond, and the increase of Co^{3+} production, thus improving the OER electrocatalytic performance [50]. PBA is used as a typical coordination compound, and the heat treatment deligandation-conversion strategy has not been widely used.

In this study, we prepared spherical CFP particles *via* a chemical deposition method. The ratio of Co^{3+}/Co^{2+} can be controlled through the heat treatment of the CFP precursor at different temperatures in N_2 atmosphere. The low-temperature pyrolysis preserved the three-dimensional framework of PBA, which facilitated the electron transfer and ion transfer during OER reaction (Scheme 1). Compared with other temperature-treated materials, the CFP-200 obtained at 200 °C has the highest Co^{3+}/Co^{2+} ratio, showing the best OER electrocatalytic performance.

CFP was synthesized by simple chemical deposition at room temperature. In order to determine the heat treatment temperature, thermogravimetric analysis (TG) was used to detect the change of CFP in nitrogen atmosphere (Fig. S1 in Supporting information). The TGA curve shows that the sample has two main stages of weight loss. One of the weight loss is about 200 °C, which

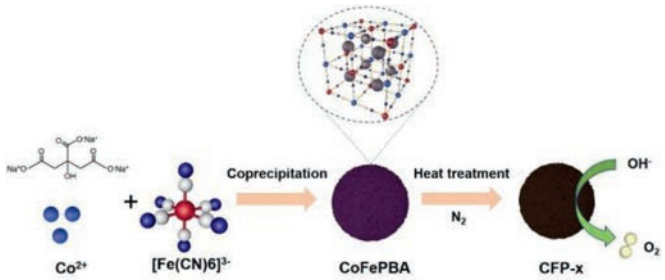

Scheme 1. Schematic illustration of the fabrication of CFP-derived samples.

is caused by the physical adsorption loss and the loss of coordination water molecules. The other weight loss is at 200–500 °C, and this is because the ligand of CFP is decomposed, causing the collapse of crystal structure. Therefore, we control the calcination temperature between 150–450 °C. CFP-x (CFP-x, x stands for temperature) was obtained *via* heat treatment of CFP at different temperatures (150, 200, 250, 300, 350, 400 and 450 °C) for 2 h in N_2 atmosphere.

The morphology of the samples was analyzed by field emission scanning electron microscopy (FESEM). Figs. 1a and b show that CFP is composed of spherical particles with a rough surface and the size of the particles is about 500–700 nm. Figs. 1f and g are the SEM pictures of CFP-200. After low-temperature heat treatment, there is no obvious change in morphology and size. Fig. S2 (Supporting information) is the SEM photographs of CFP (Fig. S2a) and CFP-x. When the heat treatment temperature is lower than 300 °C, CFP-x maintains a uniform spherical structure (Figs. S2b–e). For CFP-350, the spherical structure collapsed to a certain extent (Fig. S2f in Supporting information). For CFP-400, the spherical structure has been destroyed completely, forming a large number of nanoparticles (Fig. S2g). For CFP-450, the nanoparticles further fuse and grow, forming irregular particles (Fig. S2h). Through the transmission electron microscope (TEM), it can be observed obviously that CFP (Figs. 1c and d) and CFP-200 (Figs. 1h and i) are solid structures. The selected-area electron diffraction (SAED) characterization shows that both CFP (Fig. 1e) and CFP-200 (Fig. 1j) have a single crystal structure, and also indicates that the large particles of CFP and CFP-200 are not formed by the accumulation of nanoparticles. The structure is probably formed by a certain degree of corrosion of common PBA cubic single crystal particles. The EDS element mapping diagram shows that the components of CFP and CFP-200, including Co, Fe, C, N and O, were evenly distributed in the particle (Figs. 1k and l). In order to determine the phase information of the samples before and after heat treatment, the samples were characterized by X-ray diffraction (XRD). The XRD spectra of CFP and CFP-x are shown in Fig. 2a. There are two distinct PBA phases in the precursor. When the heat treatment temperature is lower than 350 °C, CFP-x shows a single-phase structure, and the strong diffraction peak indicates that the sample has good crystallinity. This is possible because the presence of water molecules in one of the two phases of the precursor, and the loss of water molecules after heat treatment results in only a single-phase diffraction peak. For CFP-400, the XRD pattern shows that the peaks of cobalt-ironalloy can be observed and the diffraction peaks of PBA are also maintained, indicating that CFP has been partially transformed. As shown in Fig. S4 (Supporting information), the main phase of CFP-450 is $Co_{0.7}Fe_{0.3}$ alloy, accompanied by some oxides, indicating that PBA has been completely transformed (Fig. S4).

Fourier transform infrared spectroscopy (FTIR) was used to characterize the changes of the material structure during heat treatment (Table S1 in Supporting information). As shown in

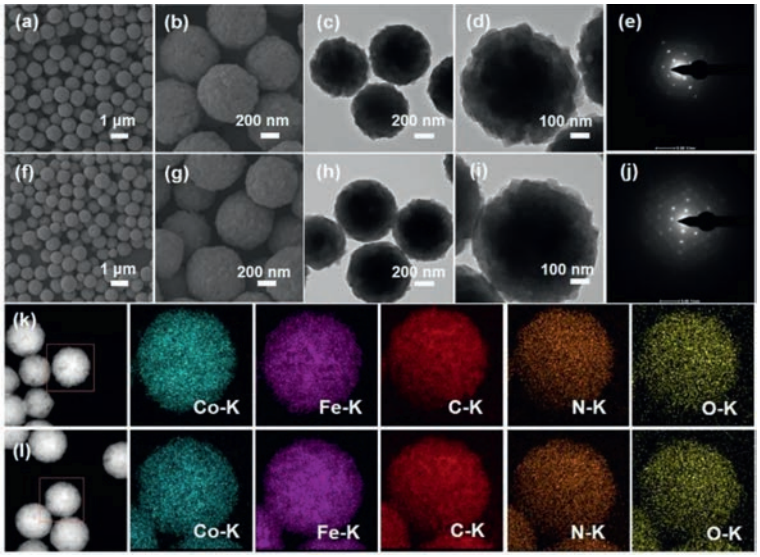

Fig. 1. Morphology and structure characterization. (a, b) FESEM, (c, d) TEM images and (e) SAED patterns of CFP. (f, g) SEM, (h, i) TEM images and (j) SAED patterns of CFP-200. EDS mapping images of Co, Fe, C, N and O in (k) CFP and (l) CFP-200.

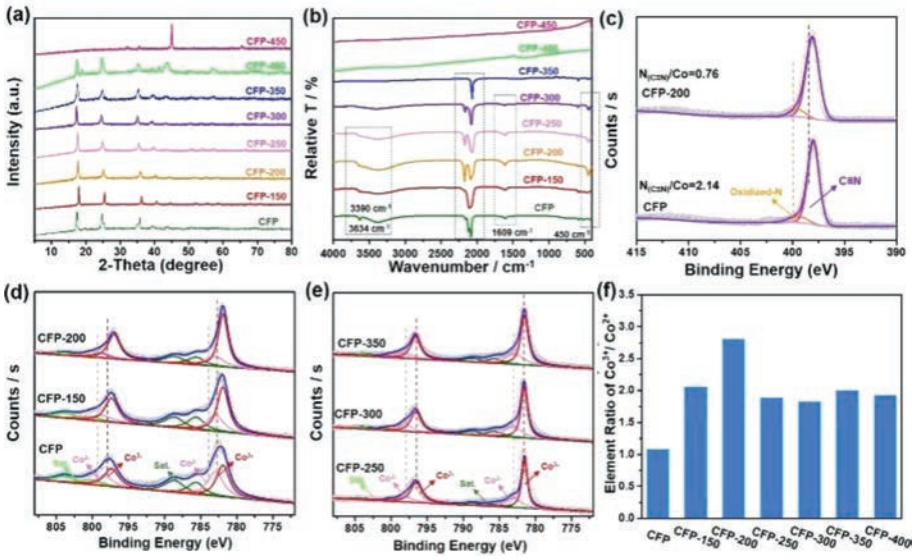

Fig. 2. (a) XRD patterns and (b) FTIR spectra of CFP and CFP-x. (c) N 1s XPS spectra of CFP and CFP-200. (d, e) High-resolution Co 2p XPS spectra of CFP and CFP-x. (f) Element ratio of Co^{3+}/Co^{2+} in CFP and CFP-x.

Fig. 2b, CFP has a relatively strong peak at 3634 cm^{-1}, indicating a part of water molecules inside the PBA crystal lattice. However, there is no obvious peak at this position for the samples after heat treatment. The peaks near 3390 cm^{-1} and 1609 cm^{-1}correspond to the absorption peaks of -OH stretching vibration and bending vibration in water molecules, respectively. These two absorption peaks cannot be observed when the heat treatment temperature is above 300 °C. The absorption peak of 2000–2200 cm^{-1} corresponds to the stretching vibration of C≡N [51,52]. When the heat treatment temperature is higher than 350 °C, there is no absorption peak in this range, indicating the PBA skeleton has completely changed when the temperature is too high. The peaks at about 450 cm^{-1} correspond to the absorption peak of bending vibration of Co^{3+}-CN. The intensity of CFP-200 is the most significant. When the heat treatment temperature is above 350 °C, the absorption peak of Co^{3+}-CN disappears, which further indicates that the PBA skeleton collapses when the temperature is too high. The main peaks of CFP can be divided into two subpeaks at 2117 and 2073 cm^{-1}. These two subpeaks correspond to the stretching vibrations of Co(III)-C≡N-Fe(II) bonds and Co(II)-C≡N-Fe(III) bonds, respectively. The CN peak of CFP-200 is composed of two main peaks. The one is 2171 cm^{-1}, corresponding to the stretching vibration of Co(II)-C≡N-Fe(III) bonds. The other can also be divided into two subpeaks at 2090 and 2053 cm^{-1}, respectively, both corresponding to the stretching vibration of Co(II)-C≡N-Fe(II) bonds. Moreover, the vibration intensity increases with the increase of temperature. The Co(II) and Fe(III)-based compounds are used as reaction precursors, which means that electron transfer occurs within the molecule of Co(II)-C≡N-Fe(III) after the formation of Co(II)-C≡N-Fe(III) [53,54].

Raman spectra of CFP and CFP-x are shown in Fig. S5 (Supporting information). Consistent with the previous characterization results, the skeleton structure of CFP was still maintained when the heat treatment temperature was lower than 400 °C. The Raman displacement between 450–650 cm^{-1} corresponds to the stretching vibration of Fe-C and Co-N and the bending vibration of Fe(Co)-

CN. The Raman displacement at about 2100 cm^{-1} corresponds to the bending vibration of -CN group. In addition, CFP-450 has two distinct Raman activity peaks at 1350 and 1596 cm^{-1}, which represent the D band and G band of the carbon structure, indicating that the carbonization has occurred at 450 °C. Since CFP has a strong absorptive capacity in the UV-visible range [55], UV-visible spectroscopy is also used for characterization (Fig. S6 in Supporting information). When the pyrolysis temperature is low, CFP shows strong absorption at about 360 nm, and a wide charge transfer band at 450–550 nm. When the pyrolysis temperature reaches 450 °C, the full absorption can be shown in the ultraviolet visible range. This is because the formation of carbon, which is consistent with the Raman results.

In order to further elucidate the changes of elemental composition and electronic state caused by heat treatment, the samples were characterized *via* X-ray photoelectron spectroscopy (XPS). Fig. S7 (Supporting information) shows the XPS full spectrum of CFP and CFP-x It can be seen that the main elements in the sample are Co, Fe, C, N and O elements, which are consistent with the EDS mapping results (Figs. 1k and l). From the N 1s XPS spectrum (Fig. 2c), the main form of N is CN, which comes from $[Fe(CN)_6]_3$ anion, and the other form is oxidized N produced during the chemical deposition under air. After relevant analysis and calculation, it can be seen that the value of N(C≡N)/Co of CFP-200 is significantly less than CFP (Fig. S8 in Supporting information), indicating that part of the skeleton of PBA collapsed during heat treatment. This is due to the loss of partial ligand destroys the Co^{3+}-CN-Fe^{2+} bond and increases the content of Co^{3+}. The Fe 2p spectra are shown in Fig. S9 (Supporting information). When the heat treatment temperature is lower than 400 °C, it can be seen that the valence states of Fe ions are +3 and +2 (Figs. S9a–c). When the pyrolysis temperature is 450 °C, Fe element shows the valence states of +3, +2 and zero (Fig. S9d). Combined with the XRD results, it further proves that the alloy is formed at a high temperature. The Co 2p spectra are shown in Figs. 2d and e and Fig. S10 (Supporting information). The spin interaction of the electrons in the Co 2p orbital causes the $2p_{1/2}$ and $2p_{3/2}$ splitting into the typical $2p_{1/2}$ and $2p_{3/2}$ double peaks. The characteristic fitting peaks at about 798.53 and 782.92 eV belong to Co^{2+}, and the characteristic fitting peaks at 797.37 and 781.94 eV belong to Co^{3+}, corresponding to their satellite peaks at the side of high binding energy. The ratio of Co^{3+}/Co^{2+} was calculated and compared through XPS, and CFP-200 had the largest ratio of Co^{3+}/Co^{2+} among all samples (Fig. 2f). Combined with other characterization, it can be concluded that the skeleton of CFP has collapsed and the structure has changed significantly when the temperature is 400 and 450 °C. Combined with XRD characterization, CFP has been partially transformed into the cobalt-iron alloy under 400 °C heat treatment. CFP has been transformed into the cobalt-iron alloy completely under 450 °C heat treatment. Combined with XPS peak division fitting, Figs. S10a and b show that the peaks at 780.14 and 796.40 eV belong to metal Co, The Co^0 of CFP-450 has a larger peak area. The high ratio of Co^0/Co indicates that CFP is transformed mostly into alloy, which is consistent with the XRD results.

Furthermore, the CFP and CFP-200 were characterized by N_2 adsorption-desorption analysis. Fig. 3 shows the N_2 adsorption-desorption isotherms and the corresponding pore structure parameters. The Brunauer-Emmett-Teller (BET) specific surface area of the CFP sample is significantly decreased after heat treatment. It is possible that the ordered microporous structure of CFP was partially destructed during heat treatment. With the increase of heat treatment temperature, the micropore area and volume decreased rapidly, and the average pore size increased significantly, which further verified the partial collapse of the CFP micropore structure [56].

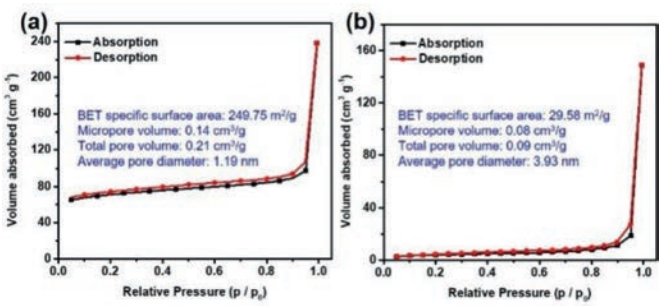

Fig. 3. N2 adsorption-desorption isotherms and pore structure parameters of samples: (a) CFP; (b) CFP-200.

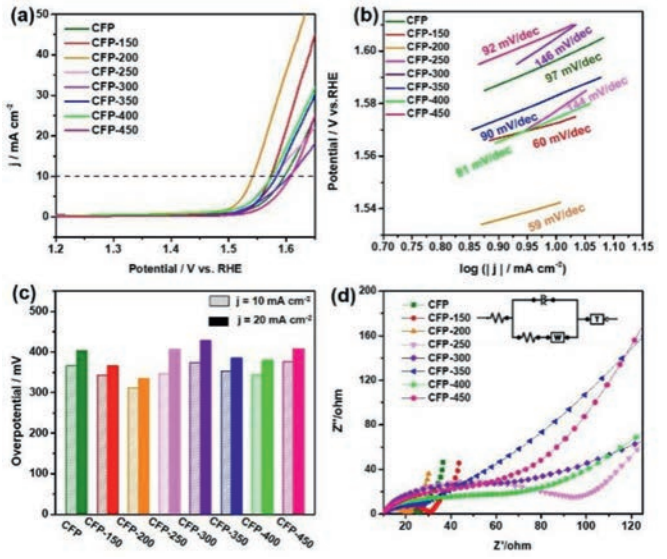

Fig. 4. LSV polarization curves for OER activity of (a) CFP and CFP-x. (b) Tafel plots from the corresponding LSV test for all samples. (c) Overpotential at 10 and 20 mA/cm^2 of all samples. (d) Nyquist plots of all samples.

In 1.0 mol/L KOH electrolyte, with a scan rate of 5 mV/s, the electrocatalytic OER activity of CFP and CFP-x was evaluated through a standard three-electrode system. Fig. 4 shows the OER performance of CFP and CFP-x at different heat treatment temperatures. The overpotential at a certain current density is often used to evaluate the OER performance of electrocatalytic materials. Fig. 4a shows the linear sweep voltammetry (LSV) graphs of different samples at a current density of 10 mA/cm^2. CFP-200 exhibits the lowest overpotential (312 mV) compared with other samples, showing the best OER performance. At the same time, at a current density of 20 mA/cm^2, the overpotential of CFP-200 is also the lowest (Fig. 4c). The Tafel slope is one of the important parameters to evaluate the kinetics of the electrocatalytic reaction process, which can further evaluate the performance of the electrocatalyst. Fig. 4b shows the Tafel curve obtained by fitting the corresponding LSV curves of all samples. It can be seen clearly that the Tafel slope of CFP-200 is only 63 mV/dec, which further confirms its high activity and shows the highest OER catalytic kinetic characteristics among all samples.

In order to further explore the charge transfer rate and interface behavior of the electrocatalyst prepared under OER circumstances, the charge transfer resistance of the sample during the OER reaction was tested to study the reaction kinetics. Fig. 4d and Fig. S12 (Supporting information) shows the corresponding Nyquist diagrams of CFP and CFP-x. All plots are composed of compressed semicircles in the high-frequency region and straight lines in the

low-frequency region. The equivalent circuit model is used to fit the curve, and the diameter of the semicircle represents the charge transfer resistance (R_{ct}) of the Faraday reaction. Most of the heat-treated samples showed a decrease in charge transfer resistance, indicating that their kinetics are accelerated in the electrocatalytic reaction. In addition, CFP-200 exhibits the smallest charge transfer resistance (R_{ct} = 10.1 Ω) in all samples, which indicated that CFP-200 has low OER overpotential and fast reaction kinetics.

High-efficiency electrocatalysts not only need to have a lower overpotential when reaching a certain current density, but also need to maintain a certain activity during long-term catalysis. As shown in Fig. S13a (Supporting information), after continuouscyclic voltammetry sweeps of 1000 cycles, the polarization curve is similar to the initial curve, and the overpotential increases only 20 mV, indicating that the catalyst has good durability in alkaline solution. In addition, the long-term catalytic stability of CFP-200 was measured by chronopotentiometry, and the IT performance test of 12,000 s and 40,000 s (Figs. S13b and c in Supporting information) further confirmed the good stability of CFP-200 in OER catalysis. The sample after the electrochemical test was characterized by SEM. For the OER catalytic reaction, due to the mixing of the electrode material and the Nafion solution, the sample morphology showed the adhesion to a certain extent. The main spherical structure remained unchanged, which further explained its stability (Fig. S15 in Supporting information).

Among all the samples, CFP-200 showed the best electrocatalytic performance. The results of the N_2 adsorption-desorption test show that the specific surface area of CFP-200 is significantly smaller than CFP. It can be considered that the Co^{3+}/Co^{2+} ratio is the most important factor to determine the catalytic performance of the material. Combined with XPS and FT-IR analysis, CFP-200 has the highest ratio of Co^{3+}/Co^{2+}. Because Co^{3+} has a higher activity than Co^{2+}, Co^{3+} has a stronger ability to oxidize H_2O and higher efficiency to O_2 generation.

In summary, a series of CFP-x samples were prepared through simple low-temperature heat treatment of CFP. XPS, FT-IR, and other characterizations confirmed the changes in the ratio of Co^{3+}/Co^{2+}. Compared with the original CFP, most of the heat-treated samples show better performance. CFP-200 with the highest ratio of Co^{3+}/Co^{2+} exhibits the best electrocatalytic activity. Through appropriate low-temperature heat treatment, the sample inherits the porous framework of CFP, which ensures the mass transfer inside the structure during the electrocatalytic OER process. Furthermore, low-temperature heat treatment induces a large amount of Co^{3+} enrichment and provides a large number of active sites. There are few reports about the exploration of the content ratio of the same metal element in different valence states *via* the low-temperature heat treatment activation method. Our research results provide a new concept and perspective for the development of high-performance electrocatalysts.

Declaration of competing interest

The authors declare no conflict of interest.

Acknowledgments

This work was supported by the National Natural Science Foundation of China (NSFC, No. U1904215), the Top-notch Academic Programs Project of Jiangsu Higher Education Institutions (TAPP), Natural Science Foundation of Jiangsu Province (No. BK20200044), Program for Young Changjiang Scholars of the Ministry of Education (No. Q2018270). Open Fund of National Joint Engineering Research Center for abrasion control and molding of metal materials (No. HKDNM2019010). We also acknowledge the Priority Academic Program Development of Jiangsu Higher Education Institutions and the technical support we received at the Testing Center of Yangzhou University.

Supplementary materials

Supplementary material associated with this article can be found, in the online version, at doi:10.1016/j.cclet.2021.08.025.

References

[1] M.G.V. Heiden, L.C. Cantley, C.B. Thompson, Science 324 (2009) 1029–1033.
[2] X. Wang, K. Maeda, A. Thomas, et al., Nat. Mater. 8 (2009) 76–80.
[3] Z. Liang, R. Zhao, T. Qiu, R. Zou, Q. Xu, EnergyChem 1 (2019) 100001.
[4] V. Palomares, P. Serras, I. Villaluenga, et al., Energy Environ. Sci. 5 (2012) 5884–5901.
[5] Z. He, C. Zhong, X. Huang, et al., Adv. Mater. 23 (2011) 4636–4643.
[6] J.H. Park, S. Kim, A.J. Bard, Nano Lett. 6 (2006) 24–28.
[7] S. Zheng, X. Guo, H. Xue, et al., Chem. Commun. 55 (2019) 10904–10907.
[8] X. Li, C. Wang, H. Xue, H. Pang, Q. Xu, Coord. Chem. Rev. 422 (2020) 213468.
[9] J. Zhang, B. Sun, Y. Zhao, et al., Nat. Commun. 10 (2019) 602.
[10] B. Li, H. Xue, H. Pang, Q. Xu, Sci. China Chem. 63 (2020) 475–482.
[11] M. Zheng, J. Jiang, Z. Lin, et al., Small 14 (2018) 1803607.
[12] J. Jiang, P. He, S. Tong, et al., NPG Asia Mater. 8 (2016) e239.
[13] D. Li, H.Q. Xu, L. Jiao, H.L. Jiang, Energy Chem. 1 (2019) 100005.
[14] Q.Y. Li, L. Zhang, Y.X. Xu, et al., ACS Sustain. Chem. Eng. 7 (2019) 5027–5033.
[15] H.F. Wang, L. Chen, H. Pang, S. Kaskel, Q. Xu, Chem. Soc. Rev. 49 (2020) 1414–1448.
[16] Z. Liang, C. Qu, D. Xia, R. Zou, Q. Xu, Angew. Chem. Int. Ed. 130 (2018) 9750–9780.
[17] Y. Xu, Q. Li, H. Xue, H. Pang, Coord. Chem. Rev. 376 (2018) 292–318.
[18] D. Sun, H. Wang, B. Deng, et al., Carbon 143 (2019) 706–713.
[19] F.C. Zhou, Y.H. Sun, J.Q. Li, J.M. Nan, Appl. Surf. Sci. 444 (2018) 650–660.
[20] Y. Jiang, S. Yu, B. Wang, et al., Adv. Funct. Mater. 26 (2016) 5315–5321.
[21] J. Qian, C. Wu, Y. Cao, et al., Adv. Energy Mater. 8 (2018) 1702619.
[22] W. Zhang, F. Zhang, F. Ming, H.N. Alshareef, EnergyChem 1 (2019) 100012.
[23] J. Liang, Y. Feng, L. Liu, et al., J. Mater. Chem. A 7 (2019) 15960–15968.
[24] H. Yi, R. Qin, S. Ding, et al., Adv. Funct. Mater. 31 (2021) 2006970.
[25] E.S. Goda, S. Lee, M. Sohail, K.R. Yoon, J. Energy Chem. 50 (2020) 206–229.
[26] Y. Li, Y. Shan, H. Pang, Chin. Chem. Lett. 31 (2020) 2280–2286.
[27] H. Duan, T. Wang, X. Wu, et al., Chin. Chem. Lett. 31 (2020) 2330–2332.
[28] B. Li, H. Pang, H. Xue, Chin. Chem. Lett. 32 (2021) 885–889.
[29] Y. Wang, Y. Wang, L. Zhang, C.S. Liu, H. Pang, Chem. Asian J. 14 (2019) 2790–2795.
[30] H.T. Bui, D.Y. Ahn, N.K. Shrestha, et al., J. Mater. Chem. A 4 (2016) 9781–9788.
[31] L. Han, P. Tang, Á. Reyes-Carmona, et al., J. Am. Chem. Soc. 138 (2016) 16037–16045.
[32] J. Shao, J. Feng, H. Zhou, A. Yuan, Appl. Surf. Sci. 471 (2019) 745–752.
[33] L. He, B. Cui, B. Hu, et al., ACS Appl. Energy Mater. 1 (2018) 3915–3928.
[34] B. Hao, Z. Ye, J. Xu, et al., Chem. Eng. J. 410 (2021) 128340.
[35] L. Zeng, L. Yang, J. Lu, et al., Chin. Chem. Lett. 29 (2018) 1875–1878.
[36] H. Liu, Y. Wang, X. Lu, et al., Nano Energy 35 (2017) 350–357.
[37] Q. Dong, Q. Wang, Z. Dai, H. Qiu, X. Dong, ACS Appl. Mater. Interfaces 8 (2016) 26902–26907.
[38] L. Xu, Q. Jiang, Z. Xiao, et al., Angew. Chem. Int. Ed. 55 (2016) 5277–5281.
[39] J. Ban, X. Wen, H. Xu, et al., Adv. Funct. Mater. 31 (2021) 2010472.
[40] Y. Sun, S. Gao, F. Lei, et al., Chem. Sci. 5 (2014) 3976–3982.
[41] Z. Ye, C. Qin, G. Ma, et al., ACS Appl. Mater. Interfaces 10 (2018) 39809–39818.
[42] H. Liu, X. Lu, Y. Hu, et al., J. Mater. Chem. A 7 (2019) 12489–12497.
[43] R. Zhu, J. Ding, Y. Xu, et al., Small 14 (2018) 1803576.
[44] R. Chen, Y. Tan, Z. Zhang, et al., ACS Sustain. Chem. Eng. 8 (2020) 9813–9821.
[45] H. Liu, X. Liu, Z. Mao, et al., J. Power Sources 400 (2018) 190–197.
[46] Y. Cheng, X. Xiao, X. Guo, H. Yao, H. Pang, ACS Sustain. Chem. Eng. 8 (2020) 8675–8680.
[47] N. Tsumori, L. Chen, Q. Wang, et al., Chem 4 (2018) 845–856.
[48] F. Qu, H. Jiang, M. Yang, Nanoscale 8 (2016) 16349–16356.
[49] Z. Zuo, Y. Li, Joule 3 (2019) 899–903.
[50] R. Zhu, J. Ding, J. Yang, et al., ACS Appl. Mater. Interfaces 12 (2020) 25037–25041.
[51] T. Shao, C. Li, C. Liu, et al., J. Mater. Chem. A 7 (2019) 1749–1755.
[52] M. Hu, S. Furukawa, R. Ohtani, et al., Angew. Chem. Int. Ed. 51 (2012) 984–988.
[53] J. Qian, C. Wu, Y. Cao, et al., Adv. Energy Mater. 8 (2018) 1702619.
[54] J.G. Wang, Z. Zhang, X. Zhang, et al., Nano Energy 39 (2017) 647–653.
[55] Y. Shi, B. Zhou, P. Wu, K. Wang, C. Cai, J. Electroanal. Chem. 611 (2007) 1–9.
[56] H. Zhou, M. Zheng, H. Tang, et al., Small 16 (2020) 1904252.